

Optimization of 3D building models by GPS measurements

Yutaro Wada¹ · Li-Ta Hsu¹  · Yanlei Gu¹ · Shunsuke Kamijo¹

Received: 24 June 2015 / Accepted: 16 November 2015 / Published online: 7 December 2015
© Springer-Verlag Berlin Heidelberg 2015

Abstract Recently, 3D building models have become an important aid to many positioning methods such as LiDAR and GPS positioning. Creating an accurate 3D building model requires accurate 2D building boundaries. We propose a method to correct the horizontal location errors of the 3D building model using GPS measurements. In an urban canyon, several GPS signals are reflected by buildings, and these reflections are potentially capable of indicating the correct position of the buildings. Starting with a raw 3D building model, we apply a signal ray tracing method to track the simulated reflection path of the GPS signal. Theoretically, the length of observed reflection path, which is known as the non-line-of-sight pseudorange, and the length of simulated reflection path should be similar. However, if the 3D map is not accurate, a difference between the pseudorange and simulated range is found. Using this difference, the proposed method estimates the true position of the wall of the 3D map. Results show that the proposed method successfully corrects the position of the wall of the raw 3D map and achieves sub-meter accuracy.

Keywords 3D building model · Building footprint · GPS · Ray tracing · Non-line of sight (NLOS) · Consistency check · Urban canyon

Introduction

Autonomous driving technologies are expected to improve driving convenience and safety. In the future, fully autonomous cars will replace human drivers. Precise localization is an essential element to realize fully autonomous driving in urban environments (Montemerlo et al. 2008; Patz et al. 2008). Furthermore, the precise localization cannot be achieved by only one type of sensor, and so both GPS and LiDAR are integrated to provide localization service with a global stability and precision, expecting sub-meter accuracy. According to the recent studies, both the localization methods of GPS and LiDAR can be improved by applying surrounding 3D models.

The most popular LiDAR-based positioning technology is simultaneous localization and mapping (SLAM) (Montemerlo et al. 2002; Smith and Cheeseman 1986). The main idea of SLAM is that the vehicle measures the positions of surrounding landmarks that are then used as a static reference for localization in the next step. However, because of the error accumulation in SLAM (Jaebum 2014), the localization with a map prepared in advance is preferable and has become a trend (Levinson et al. 2007). When the autonomous vehicle is operated on urban roads, knowledge about the vehicle position relative to the road map is needed, and positioning accuracy is expected to be sub-meter level (Gruyer et al. 2014; Nedeveschi et al. 2013). On the other hand, the more accurate positioning of landmarks is provided, the higher accuracy of vehicle localization is possibly achieved. Using GPS, accurate position estimation in urban canyon is still a challenge, with signal reflection caused by surrounding buildings leading to two effects: multipath and NLOS reception. Several methods were proposed to take advantage of the 3D map for reducing the reflection effects (Peyraud et al. 2013). One of the most

✉ Li-Ta Hsu
qmohsu@gmail.com

¹ Institute of Industrial Science, The University of Tokyo, Tokyo, Japan

common methods, the shadow matching method, uses 3D building models to predict the satellite visibility for improving the cross-street positioning accuracy (Groves 2011; Wang et al. 2013). Recently, many GPS 3D map-based approaches apply multipath and NLOS as additional measurements in the pseudorange domain (Betaille et al. 2013; Miura et al. 2015; Obst et al. 2012). Ray tracing methods are used to determine whether the transmitting path of the satellite is in line of sight (LOS) or NLOS. As a result, this GPS 3D map-based method is capable of generating the correction message for the reflection delays. We aim to generate accurate 3D building models to support accurate positioning applications.

In order to build very accurate 3D building models, there is a popular method using a mobile mapping system (MMS). A MMS uses remote sensors including camera, radar and laser to collect geographic data from the moving vehicles. The outputs of this system including GIS data, image and video are synchronized to generate the building models (Guivant and Nebot 2001; Tao and Li 2007; Yi et al. 2004). However, the expense of constructing city building models by MMS is high due to expensive equipment and heavy manual calibration. For example, the price of a commercial MMS company to construct a 3D building model in a $200 \times 200 \text{ m}^2$ area is about USD 17,000. Thus, it is difficult to generate a wide area of city building models using MMS. Another branch of the study of building 3D models is based on point cloud data from airborne laser scanners, wherein one of the steps is to automatically segment the roof of the building. In 2003, a study was released regarding automatic generation of building models by means of detecting the building roofs using aerial LiDAR data (Rottensteiner 2003). A rapid 3D building detection and modeling algorithm using aerial LiDAR data has been developed (Verma et al. 2006). Instead of detecting the building roof, the extraction of the building footprint (2D boundary) has also been proposed (Wang et al. 2006). The LiDAR point cloud data are complicated because it also includes information of trees and other infrastructure, especially in an urban area. These dense building environments became subject of a major study. In 2010, the object classification for the LiDAR data collected in urban area are discussed (Eunyoung and Medioni 2010; Pang et al. 2014). Rey-Jer and Bo-Cheng (2011) propose to reconstruct the 3D building model by integrating it with topographic maps. The potential of the combination between aerial image and LiDAR to refine the 3D building models is studied in Hermosilla et al. (2011), Susaki (2013) and Zhang et al. (2014). As for the increasing requirement of the higher accuracy 3D building models, a new classification method is also proposed to estimate building roofs accurately (Kong et al. 2014).

The objective of this research is to correct a raw 3D building model and to refine it to sub-meter accuracy. We

achieve this objective using GPS measurements. The research team in the University of Tokyo has previously developed a 3D building model-based GPS positioning method (Hsu et al. 2015; Miura et al. 2015), which implemented a ray tracing algorithm to track the signal transmitting path. We invert the positioning algorithm and propose the new method to correct the 3D building models as shown in Fig. 1.

Instead of estimating the positioning result with the aid of 3D maps, we estimate the correct 2D boundary, namely the building footprint, using a known accurate receiver position to trace the ray between the receiver, building and satellite. This is achieved by comparing the simulated result from the ray tracing method with the GPS measurements provided by the GPS receiver, which can be regarded as real signal travel path. Figure 2 demonstrates the relationship between the 3D maps and GPS measurement.

The 3D map used by ray tracing could be as accurate as ground truth if the simulation path calculated by the ray tracing algorithm is identical to the GPS observation. As shown in Fig. 2, the 3D map is gradually adjusted to the correct position by altering the ray tracing results. The raw 3D building model used is generated by combining the 2D boundary and the 3D point cloud data. The location of the generated 3D building model is in Tokyo, Japan. A commercial receiver, u-blox EVK-M8, is used to collect the GPS measurements. According to the experiment results, the proposed 2D boundary-adjusting method is capable of correcting the building model up to a sub-meter level.

An introduction of the construction of the initial and accurate 3D building model is presented first, followed by introduction of the GPS pseudorange measurement and

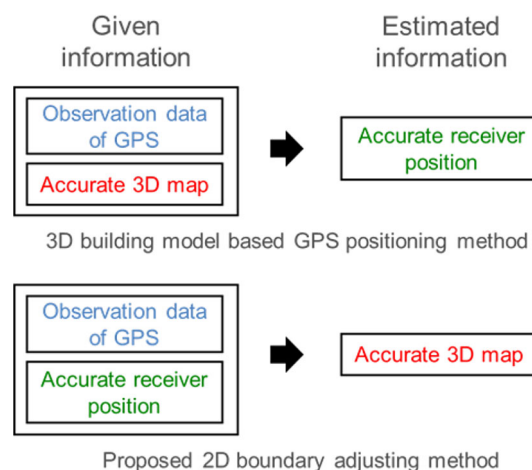


Fig. 1 Application of GPS observations for correcting 3D building models. 3D building model-based GPS positioning method is shown in the *top panel*. Proposed 2D boundary-adjusting method is shown in the *bottom panel*

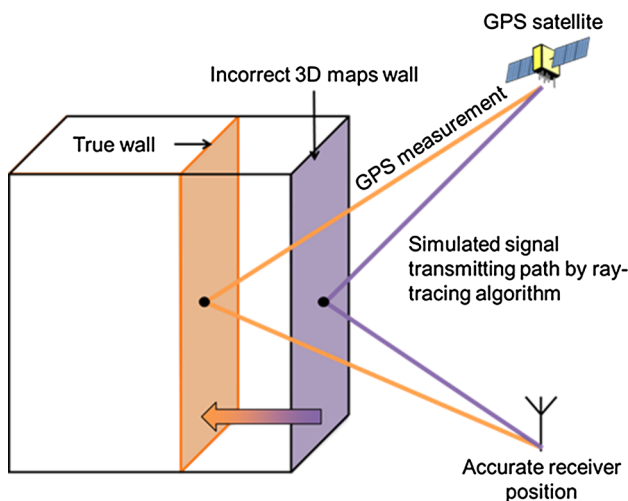


Fig. 2 Concept of applying GPS observation to correct 3D building models

simulated pseudorange generated by ray tracing. Details of the proposed 2D boundary of 3D building models correction method are introduced next, followed by the experimental setup and results. Finally, the conclusions and future work are summarized.

Construction of 3D building models

We describe the construction method of 3D building models used in our experiments, i.e., the generation of raw 3D maps that will be corrected in this research. For evaluation, accurate 3D maps are required. The accurate model used that is generated by MMS is briefly introduced.

Raw 3D building models

The proposed 2D boundary-adjusting algorithm is based on comparing the difference of the measured (actual) and simulated GPS reflection signal. The measured and simulated GPS transmitting distance are generated by the commercial GPS receiver u-blox EVK-M8 and the ray tracing method, which requires the construction of a basic

3D map, respectively. Simple shape 3D maps can be constructed by combining the information of building footprints and 3D point cloud data. The building footprint means the 2D boundary of building that can be obtained by different sources such as open-source open-street map (OSM) data or building segmentation from aerial LiDAR point cloud data. In our case, data from the fundamental geospatial data (FGD) of Japan are used as 2D geographic information system (GIS) data. Thus, the layout and position of every building on the map could be obtained from the 2D GIS data. The 3D digital surface model (DSM) data are provided by Aero Asahi Corporation. Figure 3 shows construction of the basic 3D building map (initial 3D map for the proposed method). We first extract the coordinates of every corner of buildings from FGD as shown in the left panel. Next, the 2D map is integrated with the height data from DSM. The right panel illustrates an example of a 3D map established in this research. This simple 3D building map is used as the initial 3D map.

Creating the precise 3D map by MMS

In order to evaluate the proposed method, it is necessary to have an accurate 3D map generated by a method other than the proposed method. In this study, we acquired an accurate 3D map, which is used as ground truth and was generated by MMS. This 3D map is built by A-TEC Co., Ltd, which specializes in road structure and building measurement. Table 1 shows the specifications of the commercial MMS instrument. Most of the sensors are high grade, enabling the MMS to generate accurate 3D maps. The constructed 3D maps achieve 20 cm accuracy in the horizontal.

GPS and ray tracing Algorithm

First subsection introduces the theory of generation of pseudorange measurement difference of multipath and NLOS effects in the pseudorange domain, following which the developed GPS signal ray tracing algorithm is explained in detail.

Fig. 3 Demonstration of building process of the basic 3D building models from a 2D boundary and DSM

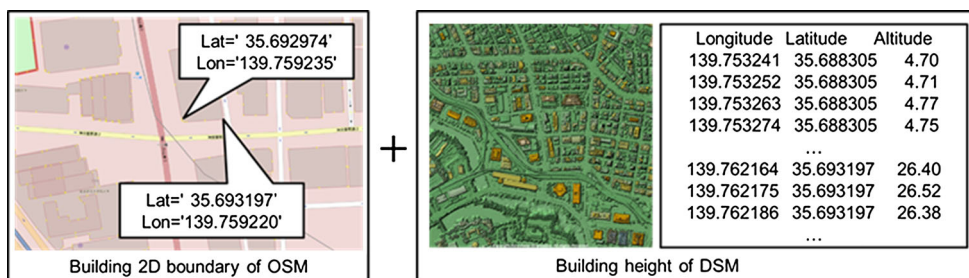
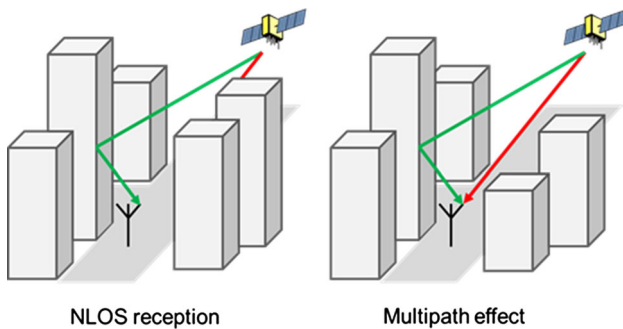


Table 1 Specifications of measuring instrument of the MMS

Instrument	Specification
Digital camera	For acquiring the road images Resolution: about 500 million pixels The distance between 2 pixels is 3 mm
Laser scanning	10 cm in traveling distance 180° area in heading direction
Travel distance	Odometer (distance meter according to the rotation of the wheel)
Positioning	Tightly coupled GNSS/INS integration system Positioning accuracy: 10 cm in horizontal accuracy, 15 cm in height accuracy
Speed	0–80 km/h

**Fig. 4** Illustration of two typical types of GPS reflection delays. NLOS reception is shown in the left panel. Multipath effect is shown in the right panel

GPS pseudorange measurement

The pseudorange ρ can be formulated by the equation below.

$$\rho(t) = r(t, t - \tau) + c\{\delta t^r(t) - \delta t^{sv}(t - \tau)\} + I_\rho(t) + T_\rho(t) + \varepsilon_\rho^{\text{refl}}(t) \quad (1)$$

where $r(t, t - \tau)$ denotes the geometric distance between the satellite and the receiver and $\delta t^r(t)$ and $\delta t^{sv}(t - \tau)$ denote the receiver and satellite clock bias, respectively. The symbol c denotes the speed of light. The symbol $I_\rho(t)$ and $T_\rho(t)$ denote the ionospheric and tropospheric delay, respectively. The symbol $\varepsilon_\rho^{\text{refl}}(t)$ denotes the pseudorange delay due to the signal reflections, typically known as multipath effects and NLOS receptions as shown in Fig. 4.

As shown in left side of Fig. 4, the NLOS reception occurs when the direct LOS signal is blocked and the signal is received only via reflections. The NLOS delay is always positive and, although typically on the order of tens of meters, is potentially unlimited. Multipath effect denotes that there are two or more traveling paths of signal from one satellite to receivers as shown in the right of Fig. 4, which leads to a pseudorange error. In comparison with the multipath effect, the calculation of the NLOS delay in

pseudorange domain is more straightforward, and it could be calculated as the reflected path minus the direct path. Therefore, we only apply the GPS measurement that suffered from the NLOS reception to correct the 3D maps. However, it is important to select the NLOS measurement from all the measurements.

Simulated pseudorange by ray tracing

The simulated pseudorange can be expressed as:

$$\hat{\rho}(t) = \hat{r}(t, t - \tau) + c\{\delta \hat{t}^r(t) - \delta \hat{t}^{sv}(t - \tau)\} + \hat{I}_\rho(t) + \hat{T}_\rho(t) + \hat{\varepsilon}_\rho^{\text{refl}}(t) \quad (2)$$

where the $\hat{\cdot}$ denotes the estimated value of the corresponding delay. The estimated geometric distance is calculated based on the ground truth position of receiver. Except the NLOS delay, all other delays can be modeled. The satellite clock offset is estimated using the QZSS L1-SAIF fast and long-term corrections (Sakai et al. 2009). The estimated ionospheric delay \hat{I}_ρ is obtained from ionospheric grid point (IGP) delay model provided by the QZSS L1-SAIF signal (Sakai et al. 2009). The estimated tropospheric delay \hat{T}_ρ is calculated based on the MOPS model (RCTA 2006). The receiver clock offset is estimated to minimize the difference between the simulated set and the measured set (Hsu et al. 2015). The NLOS delay requires tracking the signal travel path from satellite to receiver, thus creating a need for a ray tracing method. Currently, ray tracing is also used to simulate radio propagation (Hsu et al. 2015). We do not consider diffractions or multiple reflections because these signals occur under unfavorable conditions. Thus, we only utilize the direct path and a single reflected path. The developed ray tracing technique is shown in Fig. 5.

First, we generate the mirror image position of the receiver to the building surface, and then, we link the direct path between the mirror image position and satellite, namely the orange line in Fig. 5. If there is an intersection

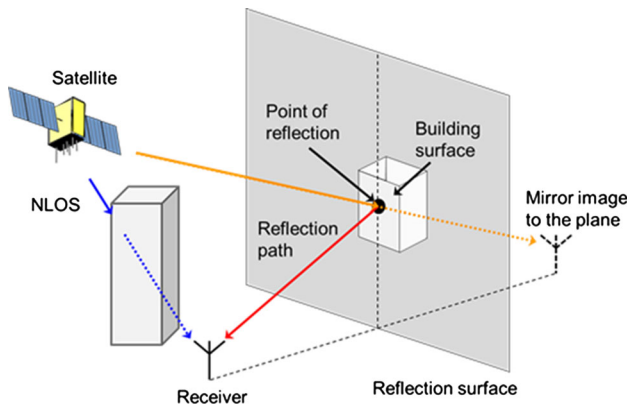


Fig. 5 Illustration of two typical types of GPS reflection delay

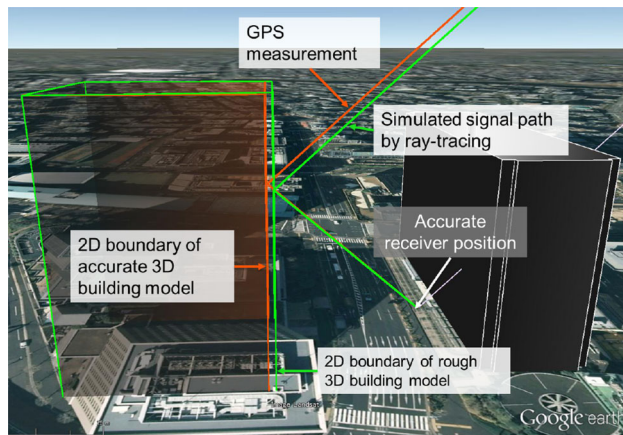


Fig. 6 Illustration of the ray tracing tracking GPS signals (Image from Google Earth)

between the direct path and the building surface, the reflection path exists from the building and vice versa. If there is no obstacle between the red path in Fig. 5 (path between the point of reflection and receiver), then the reflection can be detected. In order to identify the NLOS signal only, we need to set one more constraint to the ray tracing technique. The LOS path (blue line in Fig. 5) has to be blocked by buildings as shown in the left side of Fig. 5. Note that if more than one reflection path from the same satellite are detected, the shortest reflection path is selected. An example of the combination of the GPS signal propagation simulation using ray tracing and a 3D building map is shown in Fig. 6. Green and orange lines denote simulated NLOS path and incoming NLOS measurement, respectively. The developed ray tracing simulation can be used to distinguish reflected rays and to estimate the reflection delay distance. We assume that the surfaces of buildings are reflective smooth planes, namely mirrors. Therefore, the rays in the simulation obey the laws of reflection. Practically, the roughness and the absorption of the reflective surface might cause a mismatch between ray tracing simulation and real propagation. We neglect this

effect due to the roughness of the building surface, since it is much smaller compared with the propagation distance.

By applying the ray tracing, the reflected and obstructed direct path can be calculated. The calculation of NLOS delay is straightforward, which is the signal reflection path minus the LOS path as shown below.

$$\epsilon_{pr}^{refl} = R^{refl} - R \tag{3}$$

where R^{refl} and R denote the reflected and obstructed direct path, respectively. The simulated pseudorange plays an important role in correcting the initial 3D maps.

Proposed 2D boundary-adjusting method

Ideally, the initial 3D maps should be accurate if the simulated and measured NLOS pseudoranges are similar, i.e., the difference between the simulated and measured pseudorange becomes the smallest when the position of the wall of the initial 3D maps and the true wall positions are matched. The residual of the two pseudoranges is utilized to estimate the true position of the wall. The pseudorange residual can be expressed as:

$$d_{pr}^{n,i} = \rho^{n,i} - \hat{\rho}^{n,i} \tag{4}$$

where n and i denote the n th satellite and its reflection path which reflected by the i th wall, respectively. By classifying all the GPS observations, the pseudorange residual of each wall i can be summarized as:

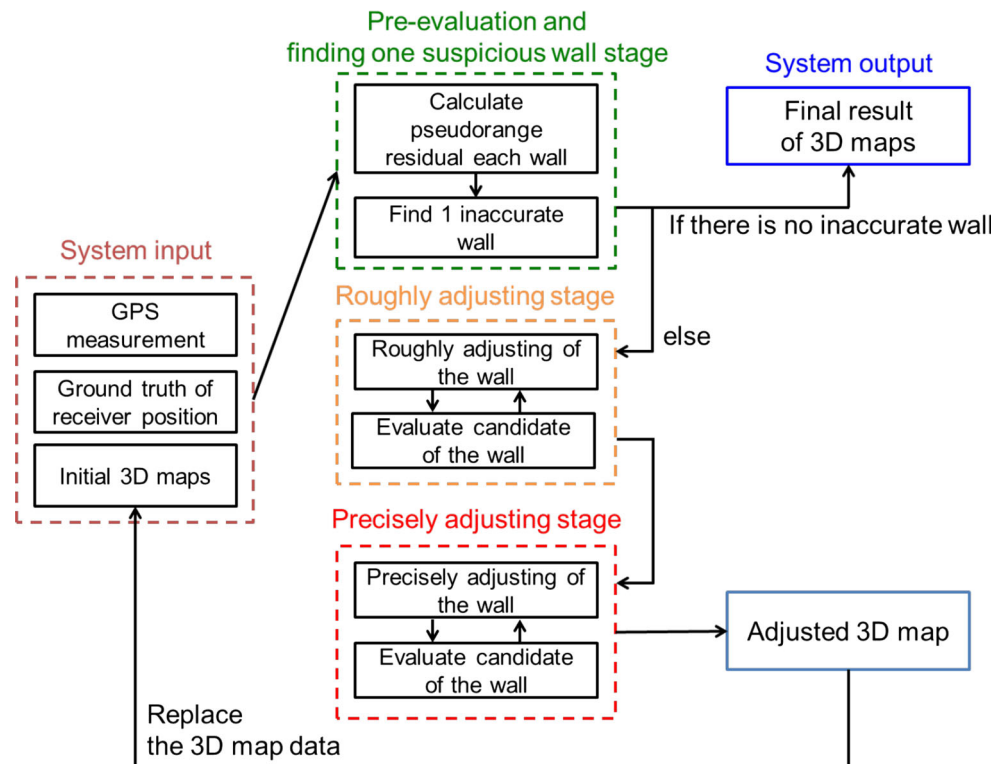
$$D_{pr}^i = \frac{1}{N_{refl}^i} \sum_n^{N_{refl}^i} |d_{pr}^{n,i}| \tag{5}$$

where N_{refl}^i denotes the total number of reflections by the i th wall. The main idea of the proposed 2D boundary-adjusting method is to adjust the wall position to reduce the pseudorange residual of each wall. The proposed method is roughly classified into three stages: (1) pre-evaluation and finding one inaccurate wall, (2) making rough adjustments and (3) making precise adjustments. The flowchart of the proposed method is depicted in Fig. 7. First, we search the walls having a detectable error and determine one of the walls to estimate its correction. Second, we estimate the approximate position of the selected wall. Finally, the approximate position of the wall is corrected. After correcting one wall, the same process is repeated by selecting a different wall. Once all the inaccurate walls are corrected, a final corrected 3D map is generated.

Pre-evaluation and finding inaccurate walls

The flowchart of detecting an inaccurate wall is shown in Fig. 8.

Fig. 7 Flowchart of the proposed 2D boundary-adjusting method algorithm



In order to find the suspicious walls, all NLOS signals have to be identified from all the GPS collected signals. We select the NLOS signal to calculate the pseudorange residual owing to its simplicity. In order to enhance the reliability of the GPS data, determination of NLOS is judged using both the received signal strength and ray tracing methods. If the results of the two LOS/NLOS determination methods are inconsistent, that satellite is excluded in the calculation. The received signal strength, which is known as carrier-to-noise ratio (C/N_0), is obtained from the GPS receiver. If the signal strength is less than 30 dB-Hz, we decide that the target satellite is NLOS. If it exceeds 40 dB-Hz, the target satellite is handled as LOS. If it is in between the upper threshold and the lower threshold, the satellite is classified only using ray tracing method, wherein the upper and the lower thresholds of the signal strength are determined empirically. In the ray tracing method, when the direct LOS line between the ground truth position of the receiver and satellite position is blocked by one of the buildings, that satellite is classified as NLOS. Conversely, if it does not touch a building, the satellite is LOS. The next step is to classify the checked NLOS signals according to the wall reflecting them. Afterward, we can calculate the difference between the simulated and measured pseudorange to obtain the pseudorange residual for

each wall. It is interesting to note that the positive/negative signs of the pseudorange residual indicate the different direction to which a wall should be shifted, as illustrated in Fig. 9.

In the case of negative sign, the position of the wall on the initial 3D map exists far from the receiver. The measured pseudorange is reflected by the true position of the wall in the real world. On the other hand, the simulated pseudorange is reflected by the position of the wall on the 3D map. The measured pseudorange is shorter than simulated one. Conversely, in the case of positive sign, the simulated pseudorange is reflected at near position of the ground truth of the receiver. It indicates that simulated pseudorange is shorter than the measured pseudorange. Ideally, all the pseudorange residuals of a same wall should be neither all negative nor all positive. However, GPS measurements are sometimes affected by many environmental factors. For example, when a tall vehicle comes near the receiver during the collection of data, the NLOS transmission path might be different from the ideally simulated path. As a result, the measured pseudorange becomes an abnormal measurement for the proposed method. By using the fact that the residuals should ideally be all positive or all negative, it is possible to exclude such abnormal measurements. To select the case, we count the

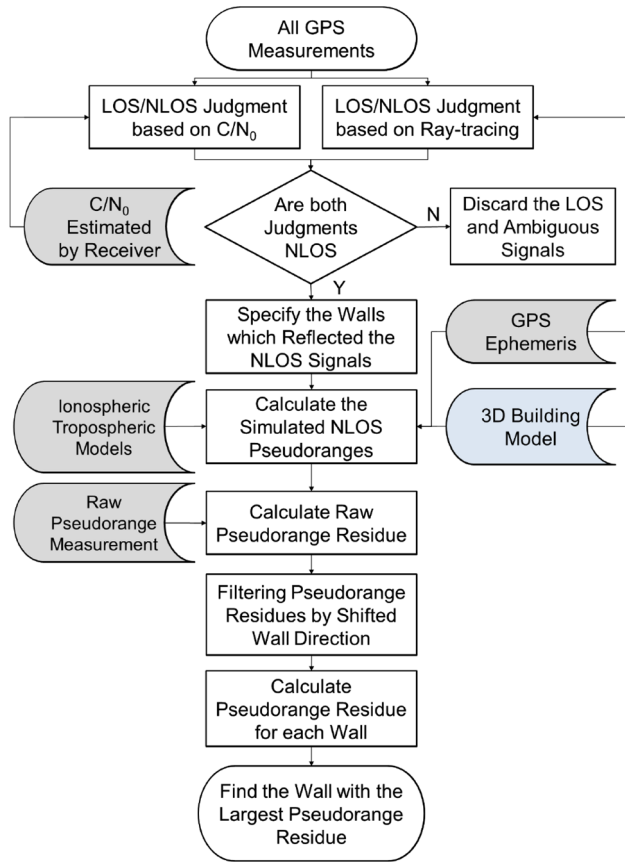


Fig. 8 Flowchart of calculating the pseudorange residual for all the walls

number of both positive and negative values and compare them to find the dominant case. For example, if there are 100 $d_{pr}^{m,i}$ in the i th wall, 80 of them are positive and 20 of them are negative, 80 positive values are used as N_{refl}^i and 20 negative values are excluded. After filtering the abnormal measurements, the pseudorange residual for each wall can be calculated by (5). Finally, the wall that has the highest \hat{D}_{pr} is selected as a target to be corrected. Figure 10 demonstrates the data exclusion by selecting the positive/negative sign of pseudorange residual. The figure shows the pseudorange residual calculated by one NLOS reflecting at the same wall, namely Eq. (4). The blue and red dots are the pseudorange residuals calculated using the initial and accurate wall position, respectively. After excluding the data in the green frame, we can calculate the mean of the pseudorange residuals for the initial and accurate wall, namely $D_{pr,init}^i$ and $D_{pr,acc}^i$. As the figure shows, ideally speaking, the $D_{pr,acc}^i$ should be zero. However, it should not be zero because of ionospheric and tropospheric residuals, and multipath effects. Importantly, the minimum D_{pr}^i achieved by adjusting the wall position is $D_{pr,acc}^i$. The next

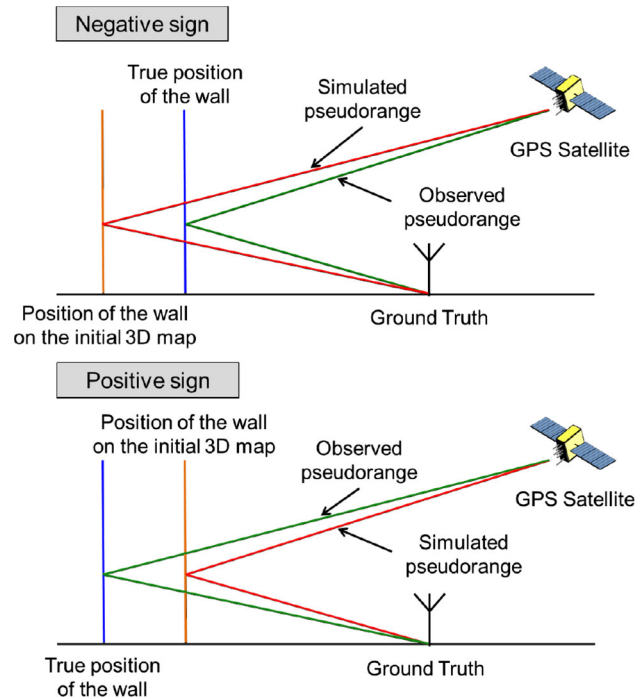


Fig. 9 Illustration of the relationship between the sign of the pseudorange residual and the shifted direction of the wall. Negative case (top), positive case (bottom)

subsection includes details on adjusting the wall of the initial 3D map according to the D_{pr}^i value.

Rough adjustment

In the rough adjustment stage, we roughly estimate the true position of the i th wall selected by the procedure described in the previous subsection. In order to adjust the i th wall, we generate the several candidates (from 1 to $j + 1$) and evaluate the pseudorange residual ($D_{pr,j}^i$) for each candidate. The flowchart of the rough adjustment stage and the demonstration of candidate distribution are shown in Fig. 11.

First, we generate the candidate wall as wall $_j^i$. The distance between each wall is defined as γ . Second, we calculate the $D_{pr,j+1}^i$ using wall $_j^i$ for estimating the roughly adjusted position of the wall. For deciding which wall candidate is close to the true wall, we compare two pseudorange residuals, $D_{pr,j}^i$ and $D_{pr,j+1}^i$. When the calculated value $D_{pr,j+1}^i$ of the epoch of the wall $_{j+1}^i$ is higher than previous value $D_{pr,j}^i$ of the previous wall $_j^i$, the previous wall $_j^i$ is selected as a roughly adjusted wall. This condition is meaningful because the smaller value of the pseudorange residual, the closer position of the wall to the ground truth position of the wall. However, if the first condition cannot be satisfied, we will check the second condition. If the difference between $D_{pr,j+1}^i$ and $D_{pr,j}^i$ is less than the

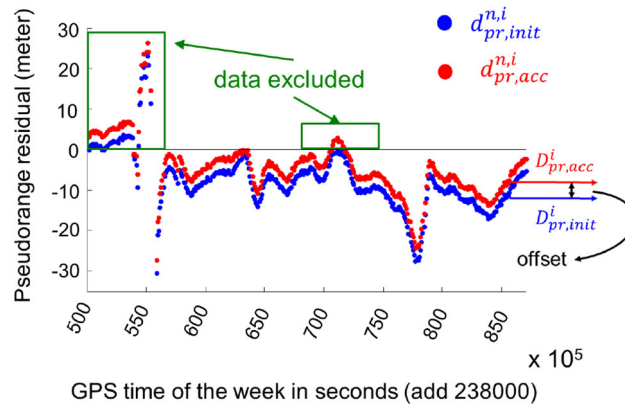


Fig. 10 Pseudorange residuals between initial wall and accurate wall. The residual of the initial wall is colored by *blue*. The residual of the accurate wall is colored by *red*

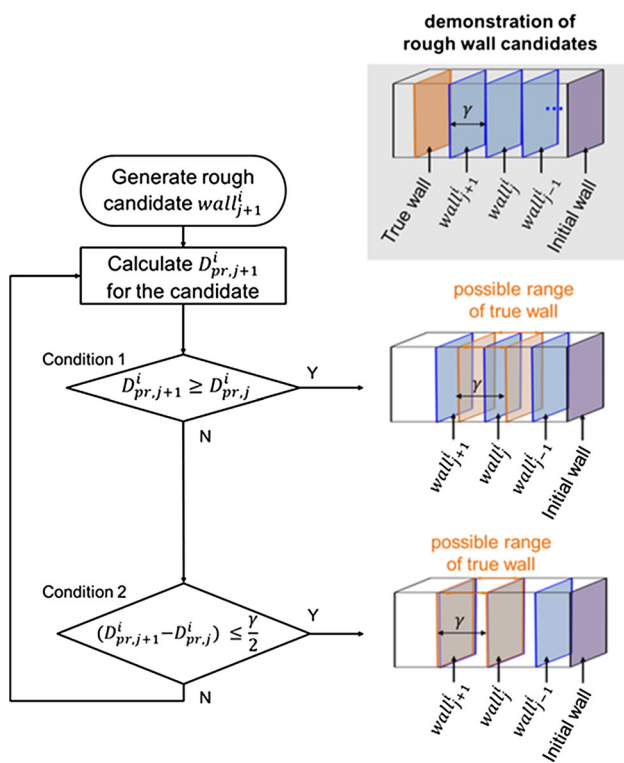


Fig. 11 Flowchart and wall candidate distribution of the rough adjustment stage

threshold value, this epoch's $wall_{j+1}^i$ is selected as a roughly adjusted wall in the second condition. In this study, we set the threshold as 0.5γ . The second condition aims to find the case that the true wall is in between the $wall_j^i$ and $wall_{j+1}^i$, as shown in the equation below:

$$|\hat{s}_{j+1} - \hat{s}_j| \leq \gamma \quad (6)$$

where \hat{s}_j denotes the distance between the truth wall and $wall_j^i$. If the difference between \hat{s}_j and \hat{s}_{j+1} is smaller than γ , the true wall is between the two walls. Thus, it is important to obtain the distances from the pseudorange residuals.

Figure 12 illustrates the relationship between the pseudorange residual and the distance. The pseudorange residual can be calculated by from the difference between measured and simulated pseudorange, which is the difference between the blue and red lines shown in the figure. As shown in the left side of the figure, the relationship can be expressed as:

$$\lim_{\theta_{j+1} \rightarrow \theta_r} \hat{s}_{j+1} \cdot \cos(\theta_{j+1} - \theta) = \hat{s}_{j+1} \cong \frac{\hat{\rho}_{j+1} - \rho}{2} \approx \frac{D_{pr,j+1}^i}{2} \quad (7)$$

where θ denotes the reflection angle of the GPS signal reflecting at the true wall. Owing to large distance between the satellite and the building, which is in the range of 20,000 km, the difference between the θ_{j+1} and θ is very small. Thus, we can obtain (7) and substitute it into (6),

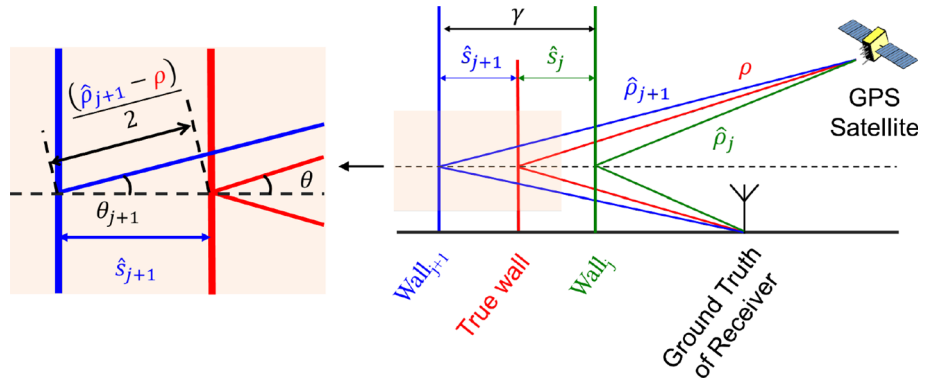
$$\left| D_{pr,j+1}^i - D_{pr,j}^i \right| \leq \frac{\gamma}{2} \quad (8)$$

As a result, if the candidate wall fulfills this second condition, the period between $wall_j^i$ and $wall_{j+1}^i$ is selected as a possible position of the true wall. Finally, the rough adjustment process is continued until one of the conditions is satisfied.

Precise adjustment

We can obtain from the rough adjustment the possible position of the true wall between two rough wall candidates. At this stage, we estimate the precise position around the possible period. First, K precise candidates of the wall are generated around the period. The width of the period is 1γ . After generating the precise candidates of the walls, we evaluate the wall at their respective positions. As a consequence, K pseudorange residuals $D_{pr,k}^i$ for each candidate are obtained. We calculate the position of precise walls based on the average of these values. This means that we

Fig. 12 Illustration of the second condition in the rough adjustment stage



need to determine the most likely position of the wall among the candidates. If the maximum value among the $D_{pr,k}^i$ is defined as $\max(D_{pr,k}^i)$, the K weights w_k are defined by following equation,

$$w_k = \frac{\max(D_{pr,k}^i) - D_{pr,k}^i}{\sum_{k=1}^K \{ \max(D_{pr,k}^i) - D_{pr,k}^i \}} \quad (9)$$

Thus, the final estimated position $wall_{est}^i$ of the i th wall is defined by

$$wall_{est}^i = \sum_{k=1}^K w_k \cdot wall_k^i \quad (10)$$

After estimating the precise i th wall, the correction of the second inaccurate wall is estimated by repeating the three stages again.

Experimental setup and results

Here, we represent the experiment results using real GPS data to correct the 3D maps. First, the experiment setups are introduced. Second, we apply the proposed method to correct the initial 3D maps, which are generated by the open-street data obtained from the FGD. Finally, the corrected 3D map is compared with the accurate 3D map generated by the MMS, and its accuracy is evaluated. GPS observation data are collected with a commercial GPS receiver. The first subsection introduces the details of our experimental setup. Afterward, we perform experiments to evaluate the wall to prove our method. The second subsection mentions the experimental details.

Experimental setup

We have used both GPS and QZSS in our method because of their high interoperability. We collected GPS observation data using the equipment. In this case, the height

between an antenna and ground is set to 3 m to avoid the effects of multipath or unintended reflection path.

We collected the data from Hitotsubashi, Tokyo, which has a high building density. The points at which GPS data are collected are shown in Fig. 13. At each green point, the observer collects data continuously for 10 min in a stationary state. The GPS observation data are collected from “Static 1” to “Static 6,” and this is repeated three times. As a result, six datasets per point were collected for 30 min. By shifting the time of recording data, we can observe the path of reflections from different walls due to the satellite movement. In this experiment, it is easy to identify the accurate position of the receiver because they were stationary. That is, we determine in advance the desirable data collection points using an aerial photograph containing latitudinal and longitudinal information. By installing the receiver on these predetermined points, it is possible to know the accurate position of the receiver.

The initial and accurate 3D maps are generated by the open-source street data and MMS, respectively. Figure 14 shows the difference between the initial and the precise 3D maps. Table 2 lists the 2D boundary error of the buildings on which we find GPS signal reflections. The minimum and maximum errors among the four buildings are about 2.7 and 1.5 m. This result indicates the 3D maps built by the public 2D GIS are not sufficiently accurate for use in positioning applications.



Fig. 13 Experiment locations to collect static data

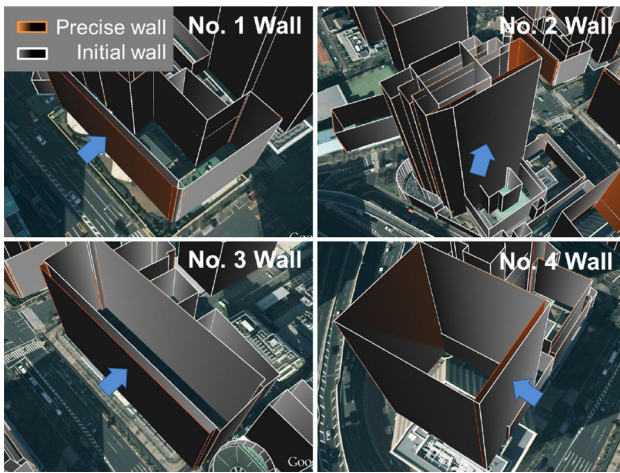


Fig. 14 Difference between the initial and the precise 3D maps (image from Google Earth)

Table 2 2D range error of the initial 3D building models

Building number	2D range error (m)
1	-1.655
2	+2.153
3	-2.739
4	+1.542

Positive value indicates direction toward the outside of the building

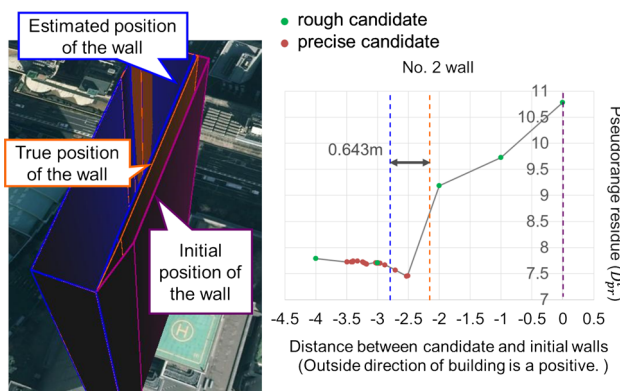


Fig. 15 Correction result of wall No. 2. The visualization of the initial, true and estimated position of the wall is presented in the *left side* (image from Google Earth). The process of adjusting the wall position using pseudorange residual is presented in the *right side*

Experimental results

In order to demonstrate the performance of the proposed method, we select five walls to correct in this experiment. Among them, there are four walls containing approximately two meters of location error. The remaining one wall is considered having no location error. The results of

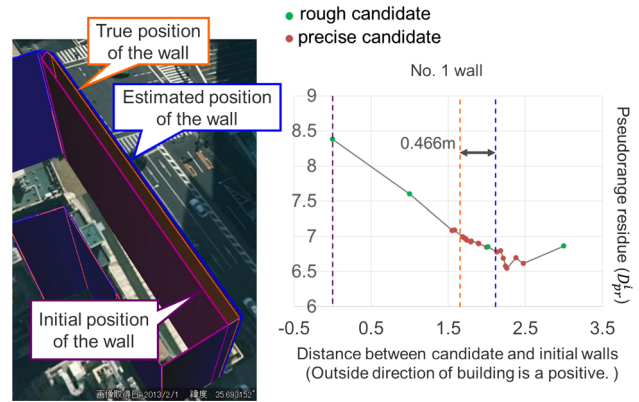


Fig. 16 Correction result of wall No. 1

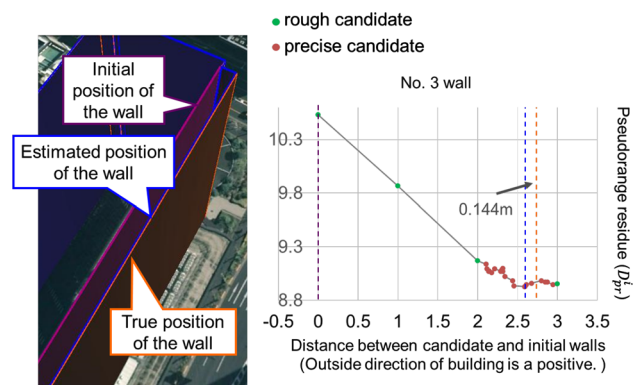


Fig. 17 Correction result of wall No. 3

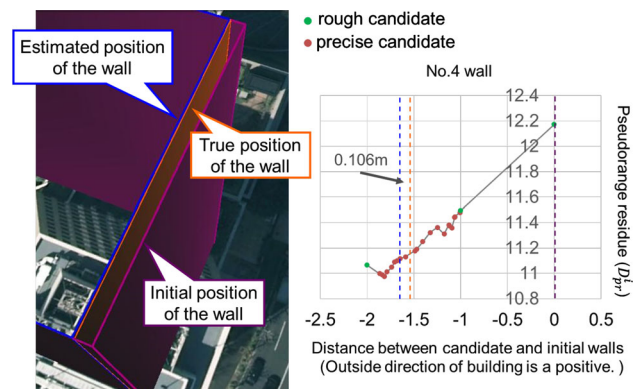


Fig. 18 Correction result of wall No. 4

applying the proposed method are shown in Figs. 15, 16, 17, 18 and 19. The order of the corrected wall is No. 2, 1, 3, 5 and 4, which is the same as the order of Figs. 15, 16, 17, 18 and 19, respectively. In these figures, the vertical axes indicate the pseudorange residual of both rough and precise candidates of the wall. The horizontal axes indicate the

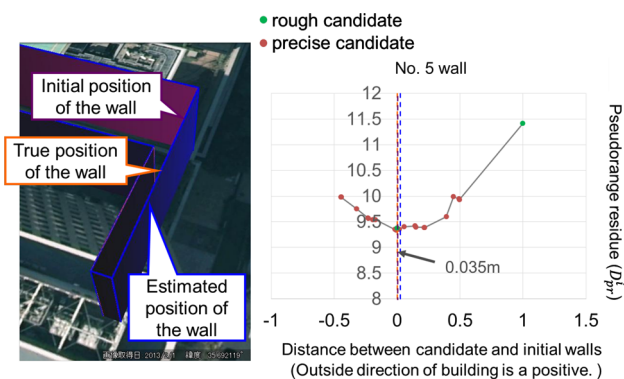


Fig. 19 Correction result of wall No. 5

Table 3 Location of the targeted wall before and after correction using the proposed method

Wall no.	Initial error	Error after correction	Improvement
1	1.655	0.466	1.189
2	2.153	0.643	1.510
3	2.739	0.144	2.636
4	1.542	0.106	0.937
5	0.000	0.035	−0.035

Units are in meters

difference between the initial position of the candidate wall and initial wall. Positive direction of the horizontal axes indicates the direction toward the outside of the true wall. Green and red points indicate the pseudorange residual of the rough and precise candidates of the wall, respectively; they are introduced in previous sections. We set the distance between two rough wall candidates, namely γ , as 1 m. The number of the precise candidates, namely K , is set as 20. Thus, the distance between two precise candidates is 0.05 m. The final estimated position of the wall is determined by solving the weighted average of these precise candidates (blue dashed lines). Also, we show a true position of the wall generated by the MMS (orange dashed lines). The distance between estimated position and true position is shown in black text. Finally, we summarize the initial error of all the selected walls and the error of the walls after the correction in Table 3.

Discussion

As shown in Fig. 15, the rough adjustment process generates five rough candidate walls for wall No. 2, namely five green points. According to the rough adjustment process, there are two conditions to terminate generation of the rough candidate wall. Comparing the pseudorange residual (D^i_{pr}) of the

candidates 4 and 5, the pseudorange residual of candidate 5 is larger than that of candidate 4, i.e., $D^{No.2}_{pr,5} > D^{No.2}_{pr,4}$, which means this No. 2 wall is terminated by condition 1. Based on condition 1, the precise candidate walls are, hence, distributed around the fourth rough candidate as shown in the right side of the figure. The final estimated position of the No. 2 wall is the blue wall as shown in the left side of the figure. The proposed method successfully reduces about 1.51 m of 2D boundary error. Note that, theoretically, the pseudorange residual of the position of true wall should be zero. However, in the real case, the pseudorange residual is not zero because the residuals of ionospheric and tropospheric error are included in it. The proposed method estimates the true position of the wall using relative pseudorange residual by comparing each pseudorange residual. Therefore, we can still estimate the true position correctly if pseudorange residual is not equal to zero.

As shown in the right side of Fig. 16, the rough adjustment of No. 1 wall is also terminated by condition 1. As shown in the left side, the proposed method reduces about 1.12 m of 2D boundary error. By observing Figs. 15 and 16, the proposed method is capable of correcting the wall in the directions perpendicular and parallel to the street.

In Fig. 17, the rough adjustment of wall No. 3 is terminated by condition 2. This indicates that the difference between the pseudorange residuals of rough candidates 3 and 4 is less than 0.5 m, i.e., $|D^{No.3}_{pr,4} - D^{No.3}_{pr,3}| \leq 0.5$. As a result, the precise candidate walls are distributed between the third and the fourth rough candidates as shown in the left side. In this case, the difference between the estimated and true walls is less than 0.15 m.

In Fig. 18, the rough adjustment of wall No. 4 is also terminated by condition 2. The error of the 2D boundary error of this wall is reduced to about 0.1 m. In brief, No. 1 and No. 2 walls satisfied condition 1, and No. 3 and No. 4 satisfied condition 2. Interestingly, the results of the walls fulfilled by condition 2 are better than those fulfilled by condition 1; reason for this can be explained by the following figure.

From Fig. 20 (top), when condition 1 is satisfied, we get a hypothesis that there is an extreme value around the $D^i_{pr,j}$; however, it is not possible to determine whether there is an extreme value in the left side (indicated by Graph A colored by blue in the Fig. 20) or the right side (indicated by Graph B colored by orange in the Fig. 20) of the graph. Therefore, we distribute the candidates of the wall around the $D^i_{pr,j}$. In other words, we cannot distribute the candidate onto the extreme value effectively. In the bottom panel, the mechanism to decide the accurate adjustment position by condition 2 is illustrated. This means that there is an

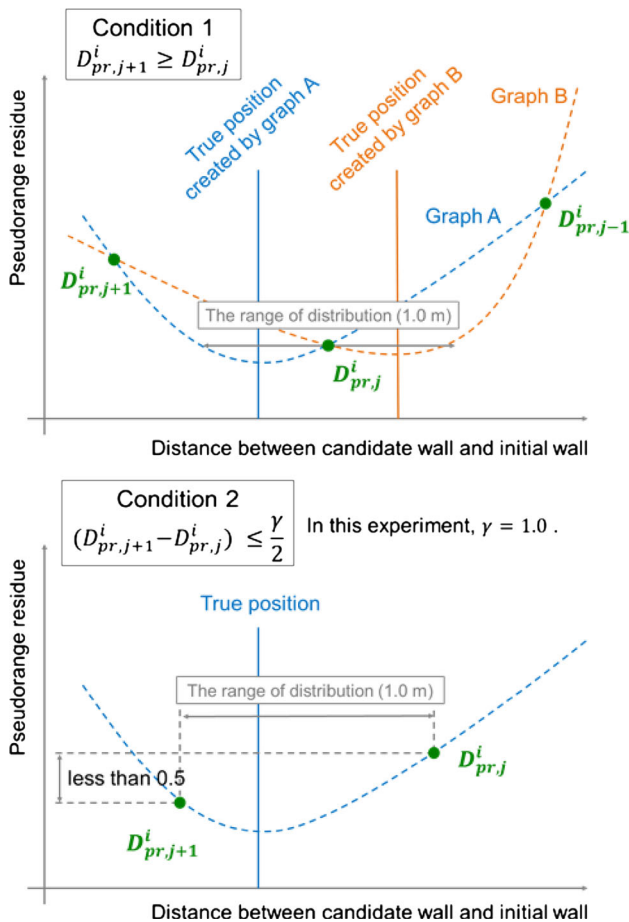


Fig. 20 Illustration of the mechanisms of the rough adjustment based on “condition 1” (top) and “condition 2” (bottom)

extreme value between $D_{pr,j+1}^i$ and $D_{pr,j}^i$, and further we can distribute the candidate onto the extreme value effectively. Thus, the result by condition 2 is better than the result by condition 1.

Finally, we test the proposed method to estimate the position of the true wall, which is estimated by MMS. In the other words, the estimated error by the proposed method should be zero. The result is shown in Fig. 19. The error after correcting by the proposed method is about 0.035 m, which is very close to the ground truth.

Conclusions

The research team of the University of Tokyo previously developed an accurate GPS positioning method based on an accurate 3D map for the urban environment. We inverted the idea of this positioning method, and instead of estimating the receiver position, we provided the true position of the receiver and used it to estimate the correct position of the 2D boundary of the buildings. By

comparing the pseudorange measurement with the simulated pseudorange, which is generated from the raw 3D map, it was possible to find the correct position of buildings. The proposed 2D boundary adjustment method consisted of three stages: (1) selecting an inaccurate wall, (2) making rough adjustments and (3) making precise adjustments. The first stage enabled locating the inaccurate buildings in the raw 3D building model. The second and third stages corrected the wall position by evaluating the generated rough and precise wall candidates. As illustrated in the experiment results, the proposed method was able to correct the building models from about 2.7 m to less than 0.5 m in terms of position error of wall. In addition, the proposed adjusting method could not only correct the biased wall, but also maintain the accurate wall. However, the proposed method is limited to correct the buildings that can reflect the GPS signals.

The work currently records the GPS signal with static receivers. In order to find more inaccurate buildings, the GPS signal should be recorded by a roving receiver; for example, a vehicle should be used to conduct the experiment. However, the number of recorded NLOS reflections in dynamic signal is much less compared with that in the static signal. A possible solution is to implement the differential GPS (DGPS) technique to obtain a cleaner pseudorange residual. In addition, the ground truth of moving vehicle trajectory is generally not as accurate as the static position. This degraded ground truth will also have an impact on the proposed method.

Acknowledgments The authors acknowledge the supports of the Grant-in-Aid for Japan Society for the Promotion of Science (JSPS) Postdoctoral Fellowship for Oversea Researchers.

References

- Betaille D, Peyret F, Ortiz M, Miquel S, Fontenay L (2013) A new modeling based on urban trenches to improve GNSS positioning quality of service in cities. *IEEE Intell Transp Syst Mag* 5(3):59–70. doi:10.1109/ITS.2013.2263460
- Eunyoung K, Medioni G (2010) Dense structure inference for object classification in aerial LIDAR dataset. In: 20th International conference on pattern recognition (ICPR), pp 3049–3052. doi:10.1109/ICPR.2010.747
- Groves PD (2011) Shadow matching: a new GNSS positioning technique for urban canyons. *J Navig* 64(3):417–430. doi:10.1017/S0373463311000087
- Gruyer D, Belaroussi R, Revilloud M (2014) Map-aided localization with lateral perception. In: IEEE intelligent vehicles symposium proceedings, pp 674–680. doi:10.1109/IVS.2014.6856528
- Guivant JE, Nebot EM (2001) Optimization of the simultaneous localization and map-building algorithm for real-time implementation. *IEEE Trans Robot Autom* 17(3):242–257. doi:10.1109/70.938382
- Hermosilla T, Ruiz LA, Recio JA, Estornell J (2011) Evaluation of automatic building detection approaches combining high resolution images and LiDAR data. *Remote Sens* 3(6):1188–1210

- Hsu L-T, Gu Y, Kamijo S (2015) 3D building model-based pedestrian positioning method using GPS/GLONASS/QZSS and its reliability calculation. *GPS Solut*. doi:[10.1007/s10291-015-0451-7](https://doi.org/10.1007/s10291-015-0451-7)
- Jaebum C (2014) Hybrid map-based SLAM using a Velodyne laser scanner. In: *IEEE 17th international conference on intelligent transportation systems (ITSC)*, pp 3082–3087. doi:[10.1109/ITSC.2014.6958185](https://doi.org/10.1109/ITSC.2014.6958185)
- Kong D, Xu L, Li X, Li S (2014) K-plane-based classification of airborne LiDAR data for accurate building roof measurement. *IEEE Trans Instrum Meas* 63(5):1200–1214. doi:[10.1109/TIM.2013.2292310](https://doi.org/10.1109/TIM.2013.2292310)
- Levinson J, Montemerlo M, Thrun S (2007) Map-based precision vehicle localization in urban environments. *Robotics: science and systems*. USA
- Miura S, Hsu L-T, Chen F, Kamijo S (2015) GPS error correction with pseudorange evaluation using three-dimensional maps. *IEEE Trans Intell Transp Syst*. doi:[10.1109/TITS.2015.2432122](https://doi.org/10.1109/TITS.2015.2432122)
- Montemerlo M, Thrun S, Koller D, Wegbreit B (2002) FastSLAM: a factored solution to the simultaneous localization and mapping problem. In: *AAAI proceedings*, pp 593–598
- Montemerlo M et al (2008) Junior: the stanford entry in the urban challenge. *J Field Robot* 25(9):569–597. doi:[10.1002/rob.20258](https://doi.org/10.1002/rob.20258)
- Nedevschi S, Popescu V, Danescu R, Marita T, Oniga F (2013) Accurate ego-vehicle global localization at intersections through alignment of visual data with digital map. *IEEE Trans Intell Transp Syst* 14(2):673–687. doi:[10.1109/TITS.2012.2228191](https://doi.org/10.1109/TITS.2012.2228191)
- Obst M, Bauer S, Wanielik G (2012) Urban multipath detection and mitigation with dynamic 3D maps for reliable land vehicle localization. In: *Proceedings of IEEE/ION PLANS*, pp 685–691
- Pang S, Hu X, Wang Z, Lu Y (2014) Object-based analysis of airborne LiDAR data for building change detection. *Remote Sens* 6(11):10733–10749
- Patz BJ, Papelis Y, Pillat R, Stein G, Harper D (2008) A practical approach to robotic design for the DARPA urban challenge. *J Field Robot* 25(8):528–566. doi:[10.1002/rob.20251](https://doi.org/10.1002/rob.20251)
- Peyraud S, Bétaille D, Renault S, Ortiz M, Mougél F, Meizel D, Peyret F (2013) About non-line-of-sight satellite detection and exclusion in a 3D map-aided localization algorithm. *Sensors* 13(1):829–847
- RCTA (2006) Minimum operational performance standards (MOPS) for global positioning system/wide area augmentation system airborne equipment, RTCA document DO-229D
- Rey-Jer Y, Bo-Cheng L (2011) A quality prediction method for building model reconstruction using LiDAR data and topographic maps. *IEEE Trans Geosci Remote Sens* 49(9):3471–3480. doi:[10.1109/TGRS.2011.2128326](https://doi.org/10.1109/TGRS.2011.2128326)
- Rottensteiner F (2003) Automatic generation of high-quality building models from lidar data. *IEEE Comput Graph Appl* 23(6):42–50. doi:[10.1109/MCG.2003.1242381](https://doi.org/10.1109/MCG.2003.1242381)
- Sakai T, Yoshihara T, Fukushima S, Ito K (2009) The ionospheric correction processor for SBAS and QZSS L1-SAIF. In: *Proceedings of the ION ITM*, pp 312–323
- Smith RC, Cheeseman P (1986) On the representation and estimation of spatial uncertainty. *Int J Robot Res* 5(4):56–68. doi:[10.1177/027836498600500404](https://doi.org/10.1177/027836498600500404)
- Susaki J (2013) knowledge-based modeling of buildings in dense urban areas by combining airborne LiDAR data and aerial images. *Remote Sens* 5(11):5944–5968
- Tao V, Li J (2007) *Advances in mobile mapping technology: ISPRS series*, vol 4. Taylor & Francis, London
- Verma V, Kumar R, Hsu S (2006) 3D building detection and modeling from aerial LIDAR data. In: *IEEE computer society conference on computer vision and pattern recognition*, pp 2213–2220. doi:[10.1109/CVPR.2006.12](https://doi.org/10.1109/CVPR.2006.12)
- Wang O, Lodha SK, Helmbold DP (2006) A Bayesian approach to building footprint extraction from aerial LIDAR data. In: *Third international symposium on 3D data processing, visualization, and transmission*, pp 192–199. doi:[10.1109/3DPVT.2006.9](https://doi.org/10.1109/3DPVT.2006.9)
- Wang L, Groves PD, Ziebart MK (2013) Urban positioning on a smartphone: real-time shadow matching using GNSS and 3D city models. In: *Proceedings of ION GNSS*, pp 1606–1619
- Yi S, Rumi W, Ying Z, Fromherz M (2004) Localization from connectivity in sensor networks. *IEEE Trans Parallel Distrib Syst* 15(11):961–974. doi:[10.1109/TPDS.2004.67](https://doi.org/10.1109/TPDS.2004.67)
- Zhang W, Wang H, Chen Y, Yan K, Chen M (2014) 3D building roof modeling by optimizing primitive's parameters using constraints from LiDAR data and aerial imagery. *Remote Sens* 6(9):8107–8133



Yutaro Wada received B.S. degree in Computer and Information Science from Tokyo University of Agriculture and Technology, Tokyo, Japan, in 2014 and is now pursuing M.S. degree in the University of Tokyo, Japan. His research theme includes self-localization in urban area with GNSS higher precision.



Li-Ta Hsu is a JSPS (Japan Society for the Promotion of Sciences) postdoctoral fellow in the Institute of Industrial Science at the University of Tokyo. He received his B.S. and Ph.D. degrees in Aeronautics and Astronautics from National Cheng Kung University in 2007 and 2013, respectively. In 2012, he was a visiting Ph.D. student in the Faculty of Engineering at University College London (UCL). He is interested in all aspects of GNSS navigation, positioning and signal processing, including wide area differential GNSS system, improving GNSS performance under challenging reception conditions, and indoor positioning techniques. He has published more than 25 papers in the associated fields.



Yanlei Gu received M.E. degree from Harbin University of Science and Technology, China, in 2008 and Ph.D. degree from Nagoya University, Japan, in 2012. He is a postdoctoral researcher in the Institute of Industrial Science at the University of Tokyo since 2013. His research interests include computer vision, machine learning and sensor integration for ITS.

smart phone applications for ITS and marketing. He is an editorial board member of “International Journal on ITS Research (Springer)” and “Multimedia Tools and Applications (Springer)” and a member of various professional organizations.



Shunsuke Kamijo received B.S. and M.S. degrees in Physics in 1990 and 1992, respectively, and Ph.D. degree in Information Engineering in 2001 from The University of Tokyo. He worked for Fujitsu Ltd. from 1992 as a processor design engineer. He was assistant professor from 2001 to 2002 and is associate professor since 2002. His research interests are computer vision for traffic surveillance by infrastructure cameras and onboard

cameras, cooperative systems using V2X communication, GNSS and

Reproduced with permission of copyright owner. Further reproduction prohibited without permission.